PCCP

ROYAL SOCIETY OF CHEMISTRY

PAPER

View Article Online
View Journal | View Issue

Cite this: *Phys. Chem. Chem. Phys.*, 2023, **25**, 17287

Mixed quantum/classical theory for rotational energy exchange in symmetric-top-rotor + linear-rotor collisions and a case study of the ND_3 + D_2 system†

Carolin Joy, Bikramaditya Mandal, Dulat Bostan and Dmitri Babikov *

The extension of mixed quantum/classical theory (MQCT) to describe collisional energy transfer is developed for a symmetric-top-rotor + linear-rotor system and is applied to ND_3 + D_2. State-to-state transition cross sections are computed in a broad energy range for all possible processes: when both ND_3 and D_2 molecules are excited or both are quenched, when one is excited while the other is quenched and *vice versa*, when the ND_3 state changes its parity while D_2 is excited or quenched, and when ND_3 is excited or quenched while D_2 remains in the same state, ground or excited. In all these processes the results of MQCT are found to approximately satisfy the principle of microscopic reversibility. For a set of sixteen state-to-state transitions available from the literature for a collision energy of 800 cm^{-1} the values of cross sections predicted by MQCT are within 8% of accurate full-quantum results. A useful time-dependent insight is obtained by monitoring the evolution of state populations along MQCT trajectories. It is shown that, if before the collision, D_2 is in its ground state, the excitation of ND_3 rotational states proceeds through a two-step mechanism in which the kinetic energy of molecule–molecule collision is first used to excite D_2 and only then is transferred to the excited rotational states of ND_3. It is found that both potential coupling and Coriolis coupling play important roles in ND_3 + D_2 collisions.

Received 11th April 2023,
Accepted 18th May 2023

DOI: 10.1039/d3cp01642k

rsc.li/pccp

I. Introduction

Collisional energy transfer (CET) is a key step in many physical and chemical phenomena that involve gas-phase molecules. In this process, energy is exchanged between translational and internal degrees of freedom of the molecules, such as vibrations and/or rotations. CET plays a significant role in probing and discerning molecular interactions. It is crucial in comprehending many processes such as combustion,[1–4] recombination reactions,[5–7] molecule–molecule[8–11] and molecule–surface inelastic scattering,[12–15] astrochemistry,[16,17] atmospheric chemistry,[18–20] photo-chemistry,[21,22] and chemistry at ultracold temperatures.[23–26]

Over the years, many experimental and theoretical studies have paved the way to broaden our understanding of the energy transfer that occurs during the collision of two molecules.[27–31] The most widely applied theoretical methods to study CET are the classical trajectory method, often referred to as the quasi-classical trajectory (QCT) method,[32–35] and the full quantum theory of molecular scattering, known as a coupled-channel (CC) formalism,[36–41] in which both the collision process and the internal states of molecules are treated using the time-independent Schrödinger equation. Despite being physically indispensable and accurate, the numerical effort attributed to the CC-formalism becomes prohibitively expensive for heavier and larger molecules and quenchers, especially at higher collision energies with many rovibrational states involved and a large number of partial waves required for the description of the scattering process.[42,43] In contrast, in QCT, the scattering process and the quantization of energy and angular momenta of the reactants are treated classically, which makes it computationally inexpensive. Unfortunately, the classical trajectory method is valid only to a certain extent. The method breaks down as the collision energy decreases and fails to account for zero-point energy (in the case of vibrational transitions in molecules),[44–47] and hence cannot be adapted to study CET between the quantized states of molecules. However, one should not rule out the possibility of formulating a theoretical approach by integrating the quasi-classical trajectory treatment of scattering with the quantum treatment of rotation and/or

Chemistry Department, Wehr Chemistry Building, Marquette University, Milwaukee, Wisconsin 53201-1881, USA. E-mail: dmitri.babikov@mu.edu

† Electronic supplementary information (ESI) available. See DOI: https://doi.org/10.1039/d3cp01642k

vibration in a self-consistent way that permits energy exchange between internal and external degrees of freedom while keeping the total energy conserved.[48,49]

During the last decade we developed such mixed quantum/classical theory (MQCT) for inelastic scattering by which the relative motion of colliding partners is described using mean-field trajectories while their internal motion (rotation and vibration) is described stringently using the time-dependent Schrödinger equation. This approach is expected to be more accurate than QCT but less costly than CC, especially when collision partners are heavy and the spectrum of internal states is dense. The accuracy and feasibility of MQCT calculations were tested in a systematic study conducted over the years by comparing their results against the results of full-quantum CC-calculations. It was found that MQCT methodology gives exemplarily accurate results for diatomic and triatomic molecules,[50–54] remains computationally feasible for polyatomic molecules colliding with atoms,[10,55] and even permits to embrace the complexity of molecule + molecule collisions.[42,56,57] Furthermore, MQCT can provide a distinctive time-dependent insight into the process,[9,55] that the standard time-independent quantum methods may not offer. Overall, MQCT turns out to be a powerful tool for describing CET in complex molecular systems in a broad range of collision energies.

In this paper we present the extension of MQCT methodology to describe a symmetric-top-rotor + linear-rotor collision process and report the results of the first application of this theory to describe CET in a ND_3 + D_2 system. Full-quantum CC-results for this process are available from recent literature[40] and can be used as a solid benchmark. Experimental studies of this process employed the technique of velocity map imaging[58] to observe correlated exchange of rotational energy between two collision partners. Excellent agreement between theoretical and experimental results was reported, which attests for the accuracy of potential energy surface (PES) and the convergence of scattering benchmark calculations.[40] Here we demonstrate that MQCT can reproduce, with good accuracy, the abovementioned correlated state-to-state transitions in two colliding molecules, which opens new opportunities for computationally efficient theoretical treatment of molecular collisions in general.

II. Theoretical approach

The rotations of each colliding partner are treated quantum mechanically and the wavefunction depends on the angles needed to describe individual orientations of these molecules. In general, for a symmetric-top molecule the rotations are described by a set of Euler angles $\Lambda_1 = (\alpha_1, \beta_1, \gamma_1)$. Following Parker,[59] we use *active* Euler rotations for each collision partner. This convention is also used in several books[60–62] and is different from *passive* rotations used by Edmonds[63] and adopted by Green.[64] Also see: Groenenboom.[65] The rotational states of the ND_3 molecule are quantized and are represented here by symmetrized combinations of Wigner D-functions:[64,66]

$$\psi_{j_1 m_1 k_1 \varepsilon}(\Lambda_1) = \sqrt{\frac{2j_1+1}{8\pi^2}}\sqrt{\frac{1}{2(1+\delta_{k_1,0})}} \times \left[D^{j_1*}_{m_1,k_1}(\alpha_1,\beta_1,\gamma_1) + \varepsilon D^{j_1*}_{m_1,-k_1}(\alpha_1,\beta_1,\gamma_1)\right] \quad (1)$$

where $\varepsilon = \pm$ is the parity index.[64,67] These states are labeled by quantum numbers $\{j_1 m_1 k_1 \varepsilon\}$ where j_1 and m_1 represent angular momentum of the first molecule and its projection onto the axis of quantization (defined below), while k_1 is the projection of j_1 on the symmetry axis of the molecule.

The rotations of a linear rotor are described by polar angles (θ,φ) and its rotational eigenstates are represented by spherical harmonics $Y^{j_2}_{m_2}(\theta,\varphi)$. Or, for convenience, one can use two of the three Euler angles:

$$\psi_{j_2 m_2}(\Lambda_2) = Y^{j_2}_{m_2}(\beta_2,\alpha_2) \quad (2)$$

where $\Lambda_2 = (\alpha_2, \beta_2, \gamma_2 = 0)$, while j_2 and m_2 represent the angular momentum of the second molecule and its projection onto the axis of quantization. Then, the coupled states of symmetric-top rotor + linear rotor can be expressed using Clebsch–Gordan (CG) coefficients $C^{j,m}_{j_1 m_1, j_2 m_2}$ as follows:

$$\Psi_{nm}(\Lambda_1,\Lambda_2) = \sqrt{\frac{2j_1+1}{8\pi^2}}\sqrt{\frac{1}{2(1+\delta_{k_1,0})}} \times \sum_{m_1=-j_1}^{+j_1} C^{j,m}_{j_1,m_1,j_2,m-m_1} \times \left[D^{j_1*}_{m_1,k_1}(\Lambda_1) + \varepsilon D^{j_1*}_{m_1,-k_1}(\Lambda_1)\right] Y^{j_2}_{m-m_1}(\Lambda_2) \quad (3)$$

Here m is the projection of total angular momentum j of the molecule–molecule system onto the axis of quantization while n is used as a composite index to label the total set of quantum numbers for the system, $n = \{j, j_1, k_1, \varepsilon, j_2\}$. The CG coefficients are nonzero only if $m = m_1 + m_2$ and $|j_1 - j_2| \le j \le j_1 + j_2$. Thus, (Λ_1, Λ_2) represent a set of quantum degrees of freedom in the system.

Time evolution of the rotational wavefunction of the system is described by expansion over a set of eigenstates:

$$\psi(\Lambda_1,\Lambda_2,t) = \sum_{nm} a_{nm}(t)\Psi_{nm}(\Lambda_1,\Lambda_2)\exp\{-iE_n t\} \quad (4)$$

where $a_{nm}(t)$ is a set of time-dependent corresponding probability amplitudes, and exponential phase factors are included to simplify solution in the asymptotic range. The value of eigenstate energy E_n depends on j_1, k_1 and j_2, but is independent of ε or total of j and m. Substitution of this expansion into the time-dependent Schrodinger equation and the transformation of wavefunctions into the rotating frame tied to the molecule–molecule vector $\vec{R}$ (used as a quantization axis in this body-fixed reference frame) leads to the following

set of coupled equations for time-evolution of probability amplitudes:[68]

$$\begin{aligned}\dot{a}_{mn''} &= -i\sum_{n'} a_{n'm} M_{n'}^{n''}(R) e^{i\varepsilon_{n'}^{n''} t} \\ &\quad - i\dot{\Phi}\Big[a_{n'',m-1}\sqrt{j''(j''+1)-m(m-1)} \\ &\quad + a_{n'',m+1}\sqrt{j''(j''+1)-m(m+1)}\Big]\Big/2\end{aligned} \tag{5}$$

Here $\varepsilon_{n'}^{n''} = E_{n''} - E_{n'}$ is the energy difference between the final and initial states of the system. Summation in the first term of this equation includes state-to-state transitions $n' \rightarrow n''$ (within each m) driven by real-valued, time-independent potential coupling matrix $M_{n'}^{n''}$:

$$M_{n'}^{n''}(R) = \langle \Psi_{n''m}(\Lambda_1,\Lambda_2)|V(R,\Lambda_1\Lambda_2)|\Psi_{n'm}(\Lambda_1,\Lambda_2)\rangle \tag{6}$$

The potential energy hypersurface $V(R,\Lambda_1,\Lambda_2)$ depends on the intermolecular distance R and the orientation of each molecule, Λ_1 and Λ_2. The second term in eqn (5) describes the $m \pm 1 \rightarrow m$ transitions (within each n) due to the Coriolis coupling effect, driven by rotation of the molecule–molecule vector $\vec{R} = (R,\Theta,\Phi)$ relative to the laboratory-fixed reference frame during the course of collision.[68]

A set of spherical polar coordinates (R,Θ,Φ) represents classical degrees of freedom in the system. They describe scattering of two collision partners relative to the laboratory-fixed reference frame and the equations for their time-evolution are obtained using the Ehrenfest theorem:[68]

$$\dot{R} = \frac{P_R}{\mu} \tag{7}$$

$$\dot{\Phi} = \frac{P_\Phi}{\mu R^2} \tag{8}$$

$$\dot{P}_R = -\sum_{n'}\sum_{n''} \mathrm{e}^{i\varepsilon_{n'}^{n''} t} \sum_m \frac{\partial M_{n'}^{n''}}{\partial R} a_{n''m}^* a_{n'm} + \frac{{P_\Phi}^2}{\mu R^3} \tag{9}$$

$$\begin{aligned}\dot{P}_\Phi &= -i\sum_{n'}\sum_{n''} \mathrm{e}^{i\varepsilon_{n'}^{n''} t} \sum_m M_{n'}^{n''} \\ &\quad \times \Big[a_{n''m-1}^* a_{n'm}\sqrt{j''(j''+1)-m(m-1)} \\ &\quad + a_{n''m+1}^* a_{n'm}\sqrt{j''(j''+1)-m(m+1)} \\ &\quad - a_{n''m}^* a_{n'm-1}\sqrt{j'(j'+1)-m(m-1)} \\ &\quad - a_{n''m}^* a_{n'm+1}\sqrt{j'(j'+1)-m(m+1)}\Big]\Big/2\end{aligned} \tag{10}$$

It appears that only the equations for R, Φ and their conjugate momenta P_R, P_Φ are needed. Since the trajectory is planar, one can restrict consideration to the equatorial plane $\Theta = \pi/2$ with $\dot{\Theta} = 0$.[52,68] Note that classical orbital angular momentum $\dot{\Phi}(t)$ drives the Coriolis transitions in the quantum equation of motion, eqn (5), while the quantum probability amplitudes $a_{nm}(t)$ create a mean-field potential in the classical equations of motion, eqn (9) and (10), providing a link between quantum and classical degrees of freedom. It was demonstrated that the total energy, which is the sum of rotational (quantum) and translational (classical), is conserved along these mixed quantum/classical trajectories.[52,68]

In principle, matrix elements of eqn (6) can be computed by a four-dimensional numerical quadrature:

$$\begin{aligned}M_{n'}^{n''}(R) &= 2\pi\int_0^\pi \sin\beta_1 \mathrm{d}\beta_1 \int_0^{2\pi} \mathrm{d}\gamma_1 \\ &\quad \times \int_0^{2\pi} \mathrm{d}\alpha_2 \int_0^\pi \sin\beta_2 \mathrm{d}\beta_2 V(R,\Lambda_1\Lambda_2)\Psi_{n''}^*(\Lambda_1\Lambda_2)\Psi_{n'}(\Lambda_1\Lambda_2)\end{aligned} \tag{11}$$

The factor of 2π comes from the analytical integration over α_1. This can be done because the potential energy of the system depends only on the relative orientations of two molecules, given by the difference $\alpha_2 - \alpha_1$. One can set $\alpha_1 = 0$, which makes $V(R,\Lambda_1,\Lambda_2)$ independent of α_1. In practice, the multi-dimensional quadrature is numerically expensive. It is better to expand $V(R,\Lambda_1,\Lambda_2)$ over a set of suitable angular functions $\tau_{\lambda_1\mu_1\lambda_2\lambda}(\beta_1,\gamma_1,\alpha_2,\beta_2)$ with R-dependent expansion coefficients $\upsilon_{\lambda_1\mu_1\lambda_2\lambda}(R)$ obtained by projecting V onto these τ-functions at each value of R within a predefined grid. These projections are also computed by numerical quadrature, but the number of expansion functions is much smaller than the number of individual matrix elements. Then, at these values of R, the potential can be represented analytically:

$$V(R,\Lambda_1,\Lambda_2) = \sum_{\lambda_1\mu_1\lambda_2\lambda} \upsilon_{\lambda_1\mu_1\lambda_2\lambda}(R)\tau_{\lambda_1\mu_1\lambda_2\lambda}(\beta_1,\gamma_1,\alpha_2,\beta_2) \tag{12}$$

For a symmetric-top rotor + linear rotor system a suitable set of functions is given by:

$$\begin{aligned}&\tau_{\lambda_1\mu_1\lambda_2\lambda}(\beta_1,\gamma_1,\alpha_2,\beta_2) \\ &= \sqrt{\frac{2\lambda_1+1}{4\pi}} \sum_{\eta=-\min(\lambda_1,\lambda_2)}^{+\min(\lambda_1,\lambda_2)} C_{\lambda_1,\eta,\lambda_2,-\eta}^{\lambda,0} \\ &\quad \times \Big[D_{\eta,\mu_1}^{\lambda_1 *}(0,\beta_1,\gamma_1) + (-1)^{\lambda_1+\mu_1+\lambda_2+\lambda} D_{\eta,-\mu_1}^{\lambda_1 *}(0,\beta_1,\gamma_1)\Big] Y_{-\eta}^{\lambda_2}(\beta_2,\alpha_2)\end{aligned} \tag{13}$$

which uses spherical harmonics Y_η^λ, Wigner D-functions and CG coefficients (see above). The meaning of indexes λ_1 (μ_1), λ_2 and λ are analogues to angular momenta for the molecule one (its projection onto the symmetry axis), the molecule two, and the entire system, respectively. Substitution of eqn (13) into eqn (12), and then into eqn (6), and a somewhat lengthy derivation outlined in the ESI,† gives the following final

expression:

$$M_{n'}^{n''}(R) = \sqrt{\frac{2j_1'+1}{2j_1''+1}}\sqrt{\frac{2j_2'+1}{2j_2''+1}}\frac{1}{\sqrt{2\left(1+\delta_{k_1',0}\right)2\left(1+\delta_{k_1'',0}\right)}}$$
$$\times \sum_{\lambda_1\mu_1\lambda_2\lambda} \upsilon_{\lambda_1\mu_1\lambda_2\lambda}(R)\sqrt{\frac{2\lambda_1+1}{4\pi}}\sqrt{\frac{2\lambda_2+1}{4\pi}}$$
$$\times C^{j_2'',0}_{j_2',0,\lambda_2,0}\sum_{m_1'=-j_1'}^{+j_1'} C^{j'',m}_{j_1',m_1',j_2',m-m_1'}$$
$$\times \sum_{\eta=-\min(\lambda_1,\lambda_2)}^{+\min(\lambda_1,\lambda_2)} C^{j'',m}_{j_1'',m_1'-\eta,j_2'',m-\left(m_1'-\eta\right)} C^{\lambda,0}_{\lambda_1,\eta,\lambda_2,-\eta} C^{j_1'',m_1'}_{j_1',m_1'-\eta,\lambda_1,\eta}$$
$$\times C^{j_2'',m-m_1'}_{j_2',m-\left(m_1'-\eta\right),\lambda_2,-\eta}$$
$$\times \left[\begin{array}{l} \left(C^{j_1'',k_1''}_{j_1',k_1',\lambda_1,\mu_1} + (-1)^{\lambda_1+\mu_1+\lambda_2+\lambda} C^{j_1'',k_1''}_{j_1',k_1',\lambda_1,-\mu_1}\right) \\ +\varepsilon'\left(C^{j_1'',k_1''}_{j_1',-k_1',\lambda_1,\mu_1} + (-1)^{\lambda_1+\mu_1+\lambda_2+\lambda} C^{j_1'',k_1''}_{j_1',-k_1',\lambda_1,-\mu_1}\right) \\ +\varepsilon''\left(C^{j_1'',-k_1''}_{j_1',k_1',\lambda_1,\mu_1} + (-1)^{\lambda_1+\mu_1+\lambda_2+\lambda} C^{j_1'',-k_1''}_{j_1',k_1',\lambda_1,-\mu_1}\right) \\ +\varepsilon'\varepsilon''\left(C^{j_1'',-k_1''}_{j_1',-k_1',\lambda_1,\mu_1} + (-1)^{\lambda_1+\mu_1+\lambda_2+\lambda} C^{j_1'',-k_1''}_{j_1',-k_1',\lambda_1,-\mu_1}\right) \end{array}\right] \quad (14)$$

In order to test the accuracy of the PES expansion method, we computed the values of matrix elements for a small subset of states that include combinations of ground and excited states of both collision partners ($j^{\pm}_{1k_1}j_2 = 1^+_1 0$, $1^-_1 0$, $2^+_1 0$, $2^-_1 0$, $3^+_1 0$, $3^-_1 0$, $1^+_1 2$, $1^-_1 2$, $2^+_1 2$, $2^-_1 2$, $3^+_1 2$, $3^-_1 2$) at two values of the molecule–molecule distance, R = 6.8 and 6.9 Bohr. In these composite state labels, the rotational levels of ND_3 are labeled as $j^{\pm}_{1k_1}$, followed by j_2 of D_2. Expansion terms with λ_1 and μ_1 up to 6, λ_2 and λ up to 4 and 10, respectively, were included in the analytic representation of the PES. Numerical quadrature was used to obtain, by projection, the expansion coefficients $\upsilon_{\lambda_1\mu_1\lambda_2\lambda}(R)$ needed in eqn (14), and to calculate the same matrix elements by direct integration using eqn (11). Equidistant grids with 40 points were used for α and γ, and a Gauss–Legendre method with 20 points was used for β. The values of computed matrix elements in this test were found to be in the range from 10^{-4} to 10^{2} cm^{-1}, but the difference between the two methods of calculations was found to be on the order of 10^{-10} cm^{-1}, from which we conclude that both methods work as expected. Direct integration of eqn (11) helps to ensure that the analytical expansion of eqn (14) is correct. The numerical speed-up of computing matrix elements by expansion is very significant, by a factor of ~11 for the subset of states indicated above.

III. Results and discussion

Within the MQCT framework, we computed state-to-state transition cross sections between the rotational states of the ND_3 + D_2 system. Following Gao *et al.*,[40] we adopted a basis set that includes the rotational levels of ND_3 up to j_1 = 8 with $k_1 \le j_1$ restricted to k_1 = 1, 2, 4, 5, 7, 8 (sometimes called "*para*" ND_3) and *ortho*-D_2 with j_2 = 0, 2, 4, which led to 138 nondegenerate quantum channels of the molecule–molecule system. Energies of these states cover the range up to $E \sim 900$ cm^{-1}. Considering all possible values of total angular momentum (up to j = 12) and its projection (in the range $-12 \le m \le 12$) resulted in 7770 quantum states overall and 1 903 543 state-to-state transitions with non-zero matrix elements $M_{n'}^{n''}$. Out of these transitions, 1 412 776 have matrix elements above 10^{-4} cm^{-1}; so, in principle, this matrix could be truncated to simplify calculations (was not implemented here because the calculations were affordable anyway). The values of matrix elements were computed on a grid of 86 points in the range of $3.5 \le R \le 25$ Bohr and interpolated using cubic spline. We carefully examined the convergence of our calculations with respect to several input parameters in the MQCT code. To ensure that symmetry properties were incorporated and taken into consideration correctly we also tried to include *ortho* states with k_1 = 0, 3, 6 for ND_3 and computed the state-to-state transition matrix elements. In this test we found that for all *ortho–para* transitions the matrix elements were numeral zeros. For simulations of collision dynamics, we started MQCT trajectories at R_{max} = 25 Bohr with impact parameters up to b_{max} = 15 Bohr and propagated the equations of motion using 4th order Runge–Kutta method with a step size of t = 50 a.u. ~1.2 fs. The relative errors of total energy conservation in eqn (7)–(10) and of the wavefunction norm conservation in eqn (5) were within 0.01% of the initial values.

The kinetic energy of ND_3 + D_2 collision was varied through a broad range from 1 cm^{-1} to 10^4 cm^{-1}. Fig. 1 gives examples of energy dependence of cross sections for several state-to-state transitions. Several more transitions are included in Fig. S1 of the ESI.† For each transition we plotted the results of "direct" MQCT calculations of quenching and excitation cross sections (solid lines), but also the results of the "reverse" approach (dashed lines), where the value of excitation cross section is derived from the computed quenching cross section, and *vice versa*, using the principle of microscopic reversibility:

$$(2j_1+1)(2j_2+1)E\sigma_{j_1j_2\to j_1'j_2'} = (2j_1'+1)(2j_2'+1)E'\sigma_{j_1'j_2'\to j_1j_2} \quad (15)$$

Here E and E' correspond to collision energies for quenching and excitation processes, respectively, of the same transition $(j_1j_2) \leftrightarrow (j_1'j_2')$ at the same total energy, so that $E = E' + \Delta E$, where ΔE is the absolute value of energy difference between states (j_1j_2) and $(j_1' j_2')$. The difference of cross sections computed using direct and reverse methods can be used to estimate the accuracy of MQCT. The data presented in Fig. 1 and Fig. S1 (ESI†) demonstrate that the microscopic reversibility is

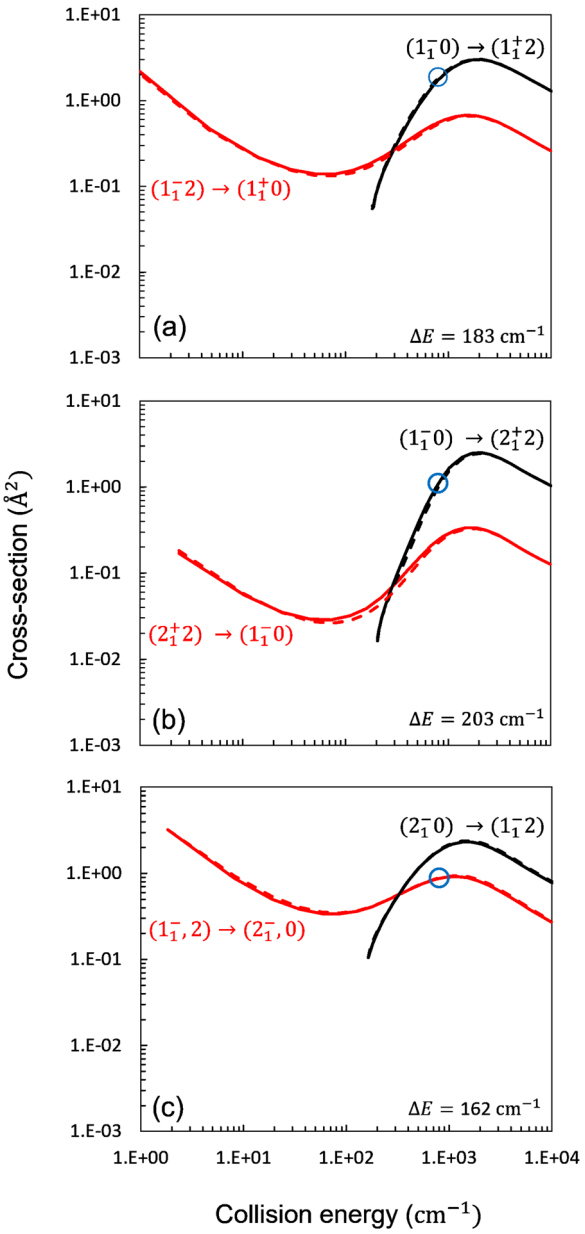

Fig. 1 The test of microscopic reversibility for transitions between several rotational states of the ND_3 + D_2 system, labeled as $(j_{1_k}^{\pm} j_2)$. Cross sections are plotted as a function of collision energy. The data obtained by "direct" MQCT calculations are shown by solid lines, whereas dashed lines represent the results of "reverse" calculations. Red color is used for quenching processes, and black color is for excitation processes. The blue symbol indicates full-quantum results of ref. 40. The value of energy difference is given for each transition.

generally satisfied in the case of MQCT calculations for all transitions in the ND_3 + D_2 system. For each excitation process presented in Fig. 1 and Fig. S1 (ESI†) the energy dependence of cross sections exhibits a very clear threshold behavior (black curves). Namely, as the collision energy is reduced and becomes merely sufficient to excite the system, the value of cross sections for the process quickly vanishes. In contrast, for all quenching processes (red curves in Fig. 1 and Fig. S1, ESI†) the value of cross section shows a steady growth towards low collision energies. One can see that at high collision energies the principle of microscopic reversibility is accurately satisfied (solid and dashed lines coincide), but some deviations can be noticed near thresholds for excitation transitions, and at very low collision energies for quenching transitions. This is expected because an approximate trajectory-based method may become less accurate at low energies.

It should be emphasized that the three transitions shown in Fig. 1 belong to three different types of processes. Namely, in Fig. 1a we deal with a nearly elastic parity-changing transition $1_1^- \leftrightarrow 1_1^+$ in ND_3 that occurs simultaneously with excitation or quenching of D_2, $0 \leftrightarrow 2$. In Fig. 1b both ND_3 and D_2 undergo the same process: either both are being excited, or both are being quenched. Finally, in Fig. 1c we see excitation of ND_3 simultaneously with quenching of D_2, and *vice versa*. Fifteen transitions presented in Fig. S1 of the ESI† are also split into these three groups. Based on this large set of data we can conclude that microscopic reversibility is satisfied reasonably well in the results of MQCT calculations for a variety of energy exchange processes and in a broad range of collision energies, except at the lowest energies where some differences are observed for some transitions (see Fig. S1, ESI†).

Also, from the data presented in the fifteen frames of Fig. S1 (ESI†) we can derive the following trend: at high collision energy the difference between excitation and quenching cross sections (the spacing between black and red curves within each frame) correlates with energy difference between the initial and final states of the ND_3 + D_2 system. The smallest difference between the excitation and quenching cross sections is found for the $4_1^{\pm}0 \leftrightarrow 1_1^-2$ transition that has the smallest energy difference of 90 cm^{-1}. The largest difference of cross sections is found for the $4_1^{\pm}2 \leftrightarrow 1_1^-0$ transition that has the largest energy difference of 275 cm^{-1}. Other transitions fall in between and follow this interesting trend. Blue symbols included in Fig. 1 and Fig. S1 (ESI†) give the values of transition cross sections from the literature, computed using the full-quantum CC method,[40] at a collision energy of 800 cm^{-1}, and we see that these data are in good agreement with our MQCT results.

In order to obtain more insight into the properties of different state-to-state transition processes in ND_3 + D_2 collisions, we plotted, for all of the transitions discussed above, the dependence of transition probabilities on collision impact parameter, sometimes called the opacity functions. The impact parameter b is related to the orbital angular momentum quantum number ℓ through the following relationship $\ell(\ell + 1) = k^2b^2$ where the magnitude of wave vector k is determined by collision energy, $\hbar k = P = \sqrt{2\mu E}$. For example, at a collision energy of 800 cm^{-1} the value of $b \sim 12$ Bohr corresponds to $\ell = 84$. Fig. 2 gives examples for three transitions out of which, again, one changes the parity of ND_3 (while D_2 is excited or quenched, Fig. 2a, d and g), second is a transition in which two collision partners undergo the same kind of change (both are either excited or quenched, Fig. 2b, e and h), and third is a transition where two collision partners exchange energy (one is excited while the other is quenched, Fig. 2c, f and i).

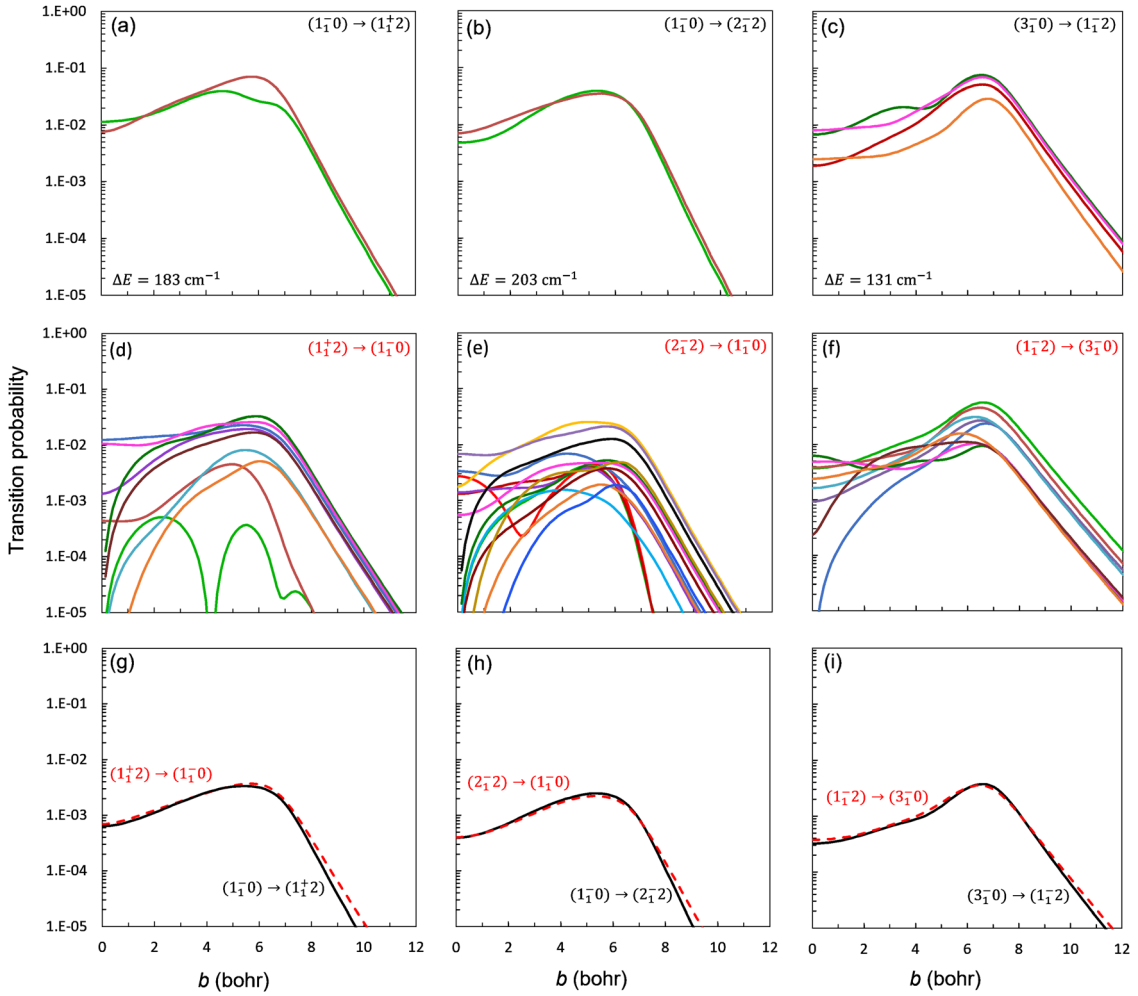

Fig. 2 Opacity functions for several transitions between the rotational states of the ND_3 + D_2 system, labeled as $(j^{\pm}_{1_k} j_2)$. Transition probabilities are plotted as a function of collision impact parameters. Collision energy is 800 cm^{-1}. In the top two rows of frames, the opacity functions are given for all individual (j,m)-components of the initial state. In the bottom row of frames, the opacity functions are averaged over the initial (j,m)-states, divided by degeneracy of the final state, and the results for excitation and quenching are plotted together, in order to check microscopic reversibility.

In the top two rows of frames in Fig. 2 different lines within the same frame correspond to different possible values of the total j and m in the initial state. For example, in the process $3_1^-0 \rightarrow 1_1^-2$ of Fig. 2c with the initial $j_1 = 3$ and $j_2 = 0$, only one initial value of total angular momentum is possible, $j = 3$, that comes with $|m| = 0$, 1, 2 and 3. This gives four different initial (j,m)-states and four curves plotted in Fig. 2c that correspond to these initial conditions. Negative values of m give the same transition probabilities as positive ones, and thus are not plotted (but they are counted in the reversibility principle, see below). However, for the reverse process $1_1^-2 \rightarrow 3_1^-0$ of Fig. 2f with the initial $j_1 = 1$ and $j_2 = 2$, three different values of total angular momentum are possible: $j = 1$, 2 and 3 that come with two, three and four values of non-negative m, respectively, which gives nine different initial (j,m)-states. So, nine curves plotted in Fig. 2f correspond to these initial states, and so on.

From Fig. 2 one can see that although all opacity functions exhibit maximum in the vicinity of the impact parameter $b \sim 6$ Bohr, it appears that, even within the same state-to-state transition, the behaviors of opacity functions for different initial (j,m)-states are quite different in the range of smaller impact parameters. Namely, for about a half of the initial (j,m)-states transition probabilities vanish in the limit $b \rightarrow 0$, while for another half of so, the probability remains significant even for impact parameter $b = 0$. For example, for the $1_1^-2 \rightarrow 3_1^-0$ transition discussed above, one opacity function (blue in Fig. 2f) vanishes in the $b \rightarrow 0$ limit, while eight others remain finite at $b = 0$. For the $1_1^+2 \rightarrow 1_1^-0$ transition, five opacity functions vanish in the $b \rightarrow 0$ limit (orange, blue, green, brown, and turquoise in Fig. 2d), while seven others remain finite at $b = 0$. Finally, for the $2_1^-2 \rightarrow 1_1^-0$ transition, seven opacity functions (blue, orange, brown, maroon, turquoise, green, and black in Fig. 2e) vanish in the $b \rightarrow 0$ limit, while seven others remain finite at $b = 0$. These two scenarios correspond to Coriolis-driven *vs.* potential-driven transition processes, respectively. It appears that, in most cases, for the same transition (say $1_1^-2 \rightarrow 3_1^-0$), matrix elements $M^{n''}_{n'}$ are non-zero only for some values of the total j and m, but turn to zero for several

other values of total j and m. In those cases when matrix elements $M_{n'}^{n''}$ are zero, the state-to-state transitions still proceed but through the Coriolis coupling, driven by the second term in eqn (5). Overall, the effect of Coriolis coupling is often smaller than potential coupling, but from transition probabilities presented in Fig. 2 one can see that in general it is not negligible and must be properly taken into account. Table S1 in the ESI† lists potential-driven and Coriolis-driven (j,m)-components for all transitions discussed in this work.

Eqn (15) above represents the principle of microscopic reversibility in terms of cross sections, but it is also instructive to write it in terms of transition probabilities of the individual MQCT trajectories, like those presented in Fig. 2. For this, it is important to recall that cross sections in eqn (15) represent the sum over final and average over initial (j,m)-states within each transition. If p represents the corresponding transition probability (summed over final and averaged over initial states), then the principle of microscopic reversibility can be rewritten as:

$$\frac{p_{j_1 j_2 \to j_1' j_2'}}{(2j_1'+1)(2j_2'+1)} = \frac{p_{j_1' j_2' \to j_1 j_2}}{(2j_1+1)(2j_2+1)} \qquad (16)$$

Probabilities in the left- and right-hand sides of eqn (16) should be obtained for the same collision impact parameter and at the same energy U of the MQCT trajectory. Note that collision energies E and E' for quenching and excitation processes that appear in eqn (15) are not anymore present in eqn (16). They analytically cancel because cross sections are inversely proportional to collision energy and proportional to transition probability, $\sigma \sim p/k^2$. In this form, left- and right-hand sides of eqn (16) represent probability per one (j,m)-state on average, *i.e.*, averaged over both final and initial states within a transition. To guarantee reversibility, these probabilities should be equal for direct and reverse processes.

In the bottom row of Fig. 2 we present these probabilities for comparison, for three transitions. Black curves were computed from the data presented in the 1st-row of frames in Fig. 2, while red curves were computed from the data presented in 2nd-row of frames in Fig. 2 (*i.e.*, for the corresponding reverse transitions). Their comparison, presented in the 3rd-row of Fig. 2, indicates a very good agreement between the two, which means that MQCT satisfies reversibility even at the level of individual trajectories. This is not immediately obvious from visual comparison of the corresponding frames in the 1st and 2nd rows of Fig. 2, because they contain a different number of curves due to different numbers of initial (j,m)-states, and, moreover, some of these curves correspond to the potential driven transitions, while others are Coriolis driven and the number of processes of each type changes from one transition to another, as one can see in Fig. 2. Still, the microscopic reversibility is satisfied in all cases! In the ESI,† we plotted the left- and right-hand sides of eqn (16) for fifteen transitions in the $ND_3 + D_2$ system in Fig. S2 (ESI†), and for fourteen more transitions in Fig. S3 (ESI†). In all these cases we observed good systematic agreement with the principle of microscopic reversibility (see the ESI†).

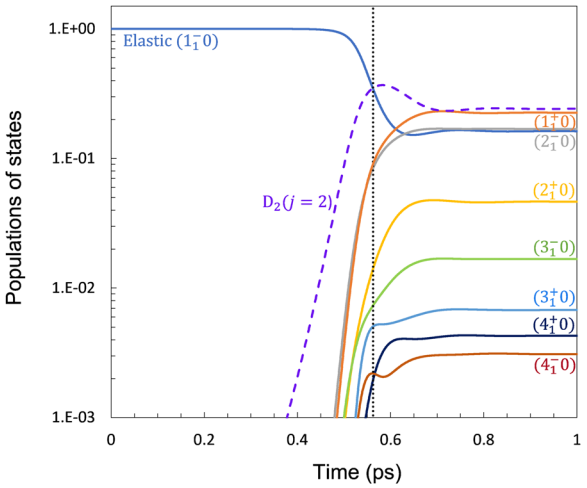

Fig. 3 Evolution of state populations in ND_3 and D_2 along one typical MQCT trajectory at a collision energy of 800 cm^{-1}. The impact parameter is b = 5.58 Bohr, which corresponds to the orbital angular momentum quantum number ℓ = 35. The initial states are ND_3 (1_1^-) and D_2 (j = 0). The total population of D_2 (j = 2) is shown by a dashed purple line. The final $ND_3 + D_2$ (j = 0) states are labeled and are indicated by color. A vertical dashed line indicates the moment of the closest approach of two molecules.

In order to obtain time-dependent insight into the process of energy exchange between two collision partners, we plotted time-evolution of state populations along the individual MQCT trajectories with chosen values of impact parameter b, indicated by small green arrows in Fig. S2 and S3 (ESI†). In Fig. 3 we present one example with collision impact parameter b = 5.58 Bohr for the initial state 1_1^-0 (the case of total j = 1 and m = 0 is shown, other cases look similar). Referring to Fig. S2 of the ESI,† one can see that the maximum values of opacity functions for several transitions are found near this value of the impact parameter, which means that the collision event presented in Fig. 3 is typical and makes a substantial contribution to the total cross section. The typical time of trajectory propagation is $\sim$1 ps, but the closest approach of two collision partners (the turning point of trajectory) happens at $\sim$0.56 ps, which represents the midpoint of the collision event, indicated in Fig. 3 by a vertical dashed line.

Analysis of Fig. 3 permits us to tell an interesting story of energy transfer in the process of ND_3 excitation by collision with D_2. One can see that the population of the initial state $ND_3(1_1^-)$ drops significantly during the collision event and this happens rather quickly, within $\sim$0.10 ps. Over 80% of the initial state population is transferred to several excited ND_3 states, but this does not happen directly. Indeed, in Fig. 3 one can notice that populations of the excited ND_3 states 1_1^+, 2_1^-, 2_1^+ and 3_1^- grow monotonically and slowly, reaching their asymptotic values on a longer time scale, $\sim$0.20 ps. During this time the excited state of D_2 (j = 2) acts as an effective intermediate state in the process of energy transfer from the translational energy of collision partners to the excited states of ND_3. Namely, the excited state of D_2 starts receiving its population early, $\sim$0.10 ps before it goes to the excited states of ND_3.

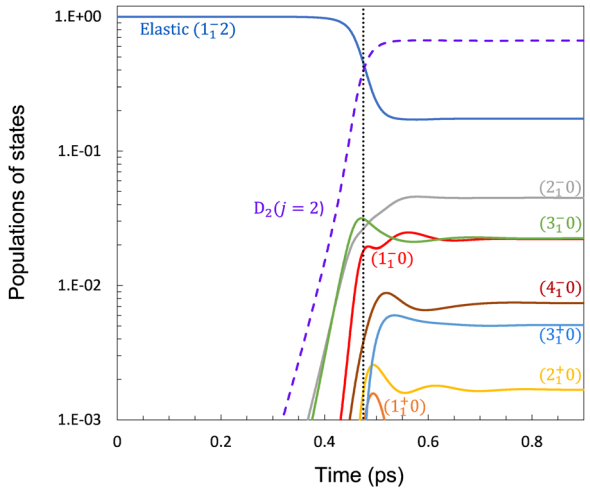

Fig. 4 Evolution of state populations in ND_3 and D_2 along one typical MQCT trajectory at a collision energy of 800 cm^{-1}. The impact parameter is b = 5.0 Bohr, which corresponds to the orbital angular momentum quantum number ℓ = 35. The initial states are $ND_3(1_1^-)$ and D_2 (j = 2). The total population of D_2 (j = 2) except elastic (1_1^-2) is shown by a dashed purple line. The final ND_3 + D_2 (j = 0) states are labeled and are indicated by color. A vertical dashed line indicates the moment of the closest approach of two molecules.

Note that in the middle of the collision event, when the population of D_2 (j = 2) becomes equal to the population of the elastic channel 1_1^-0, the populations of the excited states of ND_3 remain small, under 10%. The maximum population of D_2 (j = 2) reaches 37% but then drops to about 23%, releasing a significant portion of its population to the exited states of ND_3.

We think that the reason for the efficiency of this two-step energy transfer mechanism lies in the energy scales in the system. Namely, the excitation energy of D_2 (j = 2) is 183 cm^{-1}, while the energy spacings between the rotational states of ND_3 are much smaller: 20.57, 30.85 and 41.15 cm^{-1} between the consecutive states. The former is much closer to the kinetic energy of collision, which is 800 cm^{-1}. Therefore, the rotational states of D_2 represent a more suitable sink for a large translational energy of collision partners. The rotational states of ND_3 receive energy from the excited D_2, rather than from the translational motion directly, again, due to similar energy scales.

In Fig. 4 we present another example of evolution of individual state populations along the MQCT trajectory, for a different initial state 1_1^-2. This case permits us to see what happens when a significant amount of energy is already stored in D_2 (j = 2) prior to the ND_3 + D_2 collision. The values of total j = 1 and m = 0 were chosen for the initial state, as before. The value of the impact parameter was b = 5.00 Bohr and the moment of the closest approach of two collision partners was at ~0.47 ps. From Fig. 4 we see that in this case the populations of excited ND_3 states grow monotonically within both the excited D_2 (j = 2) and ground D_2 (j = 0) manifolds, with the excited state being ahead of the ground, both in terms of the beginning of the excitation process (that starts about ~0.05 ps earlier for the excited D_2) and in terms of the final transition probability (that is an order of magnitude larger for the excited D_2). We conclude that if the initial state of D_2 is already excited (j = 2), the process of ND_3 excitation is direct, in contrast to the two-step process discussed above for the case of ground state D_2 (j = 0).

One may also notice from Fig. 4 that in this example the populations of all positive parity states are much smaller compared to their negative parity counterparts. For example, the population of 1_1^+0 remains small during the collision event and vanishes after the collision. The population of state 4_1^+0 remains below 10^{-3}, outside of the frame in Fig. 4. This is very different from the case presented in Fig. 3, where cross sections for ND_3 states of two parities are comparable. We found that for these initial conditions (namely, total j = 1 and m = 0 of 1_1^-2 – state) the parity changing transitions to D_2 (j = 0) are Coriolis-driven. For these processes the potential coupling matrix elements $M_{n'}^{n''}$ of eqn (6) are zero due to symmetry. The time evolution of corresponding probability amplitudes is driven only by the second term in eqn (5) – the Coriolis coupling term, since the contribution of the first term (the potential coupling term) is null. It should not be mistakenly concluded, though, that all parity changing transitions are exclusively Coriolis driven. This is not the case. For example, the initial state with total j = 1 and m = 1 (of the same 1_1^-2 – channel) has non-zero potential coupling matrix elements $M_{n'}^{n''}$ that would make a significant contribution to parity changing transitions. As mentioned above, for about a half of the initial (j,m)-states the potential coupling matrix elements are zero, and in those cases the Coriolis coupling is the only mechanism.

In Fig. 5 we present one more example of the MQCT trajectory, for the initial state 2_1^-2 (total j = 0 and m = 0) and the impact parameter b = 0. This trajectory corresponds to a

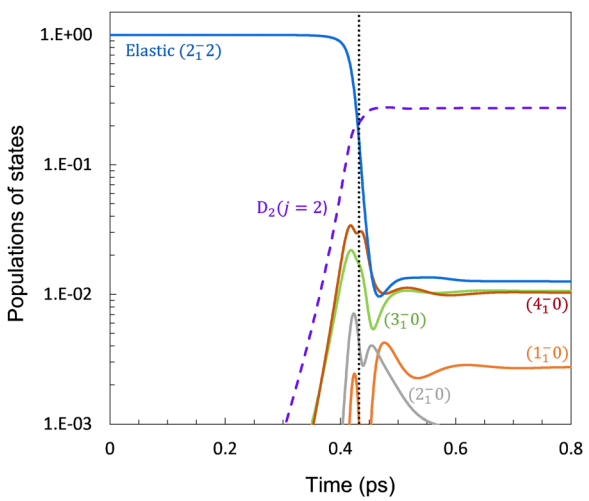

Fig. 5 Evolution of state populations in ND_3 and D_2 along one typical MQCT trajectory at a collision energy of 800 cm^{-1}. The impact parameter is b = 0, which corresponds to the orbital angular momentum quantum number ℓ = 0. The initial states are ND_3 (2_1^-) and D_2 (j = 2). The total population of D_2 (j = 2) except elastic (2_1^-2) is shown by a dashed purple line. The final ND_3 + D_2 (j = 0) states are labeled and are indicated by color. A vertical dashed line indicates the moment of the closest approach of two molecules.

head on collision with orbital angular momentum $\ell = 0$. The initial value of angular speed $\dot{\Phi}$ of $\vec{R}$-vector rotation is also zero, and it remains zero during the entire collision event. Collision partners approach each other along a straight line, reach the turning point and scatter back to the asymptotic region, all along a straight-line trajectory. In this case the contribution of Coriolis coupling is null because the corresponding term in eqn (5) has a pre-factor of $\dot{\Phi}$. Indeed, the Coriolis coupling between the quantum states in the MQCT method is driven by rotation of the molecule–molecule vector $\vec{R}$ treated classically. If $\dot{\Phi} = 0$ the vector $\vec{R}$ does not rotate at all, and there are no Coriolis coupling and no Coriolis-driven state-to-state transitions. This is exactly the case presented in Fig. 5. Therefore, for this special trajectory, there are no transitions to the states of positive parity.

One of the main goals of this paper was to compare our MQCT results with the full-quantum results of Gao *et al.*[40] It should be mentioned, though, that the labelling of rotationally degenerate states in their work is different. Namely, they label the states of ND_3 using umbrella inversion symmetry s, related to the parity index ε through the following expression: $s = (-\varepsilon)(-1)^{j_1}$, see, *e.g.*, page 483 of ref. 67 and eqn (A19) and (A20) of Green.[64] Therefore, the initial state labeled as 1_1^- is the same state both here and there, and this is true for all rotational states with odd values of j_1. But, for the states with even values of j_1 our parity index ε is opposite to their inversion symmetry s. In what follows (Fig. 6 and its discussion) we adopt their notations, to avoid confusion.

Fig. 6 represents the comparison of our state-to-state transition cross sections (obtained using MQCT) against the full-quantum data from Fig. 12 and 13 of ref. 40. The top frame gives excitation of ND_3 (1_1^-) in coincidence with excitation of D_2 $(j = 0)$, while the bottom frame gives excitation of ND_3 (1_1^-) in coincidence with quenching of D_2 $(j = 2)$. One important conclusion is that MQCT gives a reliable description of the process including all kinds of transitions and energy exchange pathways between collision partners. On a quantitative level, MQCT seems to underestimate the values of cross sections by about 8% (RMSD for a set of 16 transitions in Fig. 6), which is quite satisfactory, considering the approximate quantum/classical nature of the method. It is interesting to note that in the case of D_2 excitation, MQCT shows a larger deviation from the full quantum results (11% RMSD for 8 transitions in the top frame of Fig. 6) compared to the case of D_2 quenching (2% RMSD for 8 transitions in the bottom frame of Fig. 6).

Let us take closer look at the process in which for ND_3 only the parity changes $(1_1^- \rightarrow 1_1^+)$ while D_2 is excited or quenched $(0 \leftrightarrow 2)$. The case of D_2 excitation exhibits the largest cross section of all (see the top frame of Fig. 6), but the case of D_2 quenching exhibits a cross section that is a factor of $\sim$3 smaller (see the bottom frame of Fig. 6). The origin of this difference is due to the different natures of these two transitions. Namely, the process $(1_1^-0) \rightarrow (1_1^+2)$ corresponds to the initial $j_1 = 1$ and $j_2 = 0$, with only one initial value of total angular momentum possible, $j = 1$, that comes with $m = 0$ and ± 1. We checked and found that, for both these components, the transitions are driven by potential coupling with non-zero matrix elements $M_{n'}^{n''}$. In contrast, the process $(1_1^-2) \rightarrow (1_1^+0)$ corresponds to the initial $j_1 = 1$ and $j_2 = 2$, with three possible values of total angular momentum, $j = 1$, 2 and 3 that come with their corresponding m-states, giving nine different initial (j,m)-states. We found that out of these nine components, only four transitions are driven by the potential coupling, while five transitions are driven by Coriolis coupling alone, since the potential coupling is null. The potential-driven components are: $(j,|m|) = (1,1)$, $(2,0)$, $(2,1)$ and $(3,1)$, while the Coriolis-driven components are $(j,|m|) = (1,0)$, $(2,2)$, $(3,0)$, $(3,2)$ and $(3,3)$. On average, this makes the $(1_1^-2) \rightarrow (1_1^+0)$ process much weaker, compared to the $(1_1^-0) \rightarrow (1_1^+2)$ process where each component is driven by the potential coupling (see Fig. 6).

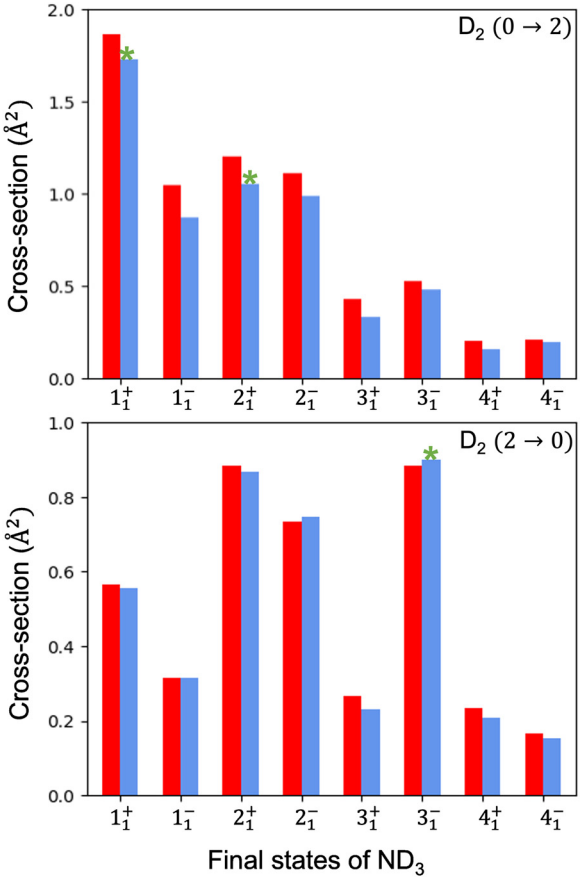

Fig. 6 Cross sections for excitation of ND_3 $(j_k^{\pm})$ states from its ground state (1_1^-) in collisions with D_2. In these processes the excitation of ND_3 occurs in coincidence with excitation (0 → 2, top frame) or quenching (2 → 0, bottom frame) of the rotational states of D_2. Our MQCT results and the full-quantum results of ref. 40 are shown in blue and red colors, respectively. Transitions labeled using asterisks are analyzed in detail in Fig. 2.

Another interesting feature one may notice in Fig. 6 is that in the top frame (where D_2 is excited) the excitations of 3_1^+ and 3_1^- states exhibit comparable cross sections, while in the bottom frame (where D_2 is quenched) the excitation of the 3_1^- state exhibits a cross section larger by a factor of three than that for the 3_1^+ state. We analyzed these processes in detail and found

that, first of all, some of the potential driven transition probabilities are larger for the $(1_1^-2) \rightarrow (3_1^-0)$ transition than for $(1_1^-2) \rightarrow (3_1^+0)$. Moreover, we found that for the $(1_1^-2) \rightarrow (3_1^-0)$ transition, eight out of nine (j,m)-components are potential-driven, and only one is Coriolis driven (see Fig. 2), whereas for the $(1_1^-2) \rightarrow (3_1^+0)$ transition seven (j,m)-components are potential-driven, while two are Coriolis driven, which makes the latter transition weaker (see the bottom frame of Fig. 6). In contrast, the corresponding transitions in the top frame of Fig. 6, $(1_1^-0) \rightarrow (3_1^+2)$ and $(1_1^-0) \rightarrow (3_1^-2)$, are characterized by two potential-driven (j,m)-components each, and thus exhibit very similar cross sections.

IV. Conclusions

In this work we presented the extension of MQCT methodology onto a symmetric-top-rotor + linear-rotor system and applied this theory to describe energy transfer in ND_3 + D_2 collisions. Calculation of matrix elements for state-to-state transitions driven by potential coupling was carried out in two complementary ways: by direct numerical multi-dimensional integration and by analytic expansion of the PES over a basis set. The two methods were found to give the same results, and a speed-up by more than an order of magnitude was observed (for the basis set expansion), which offers a fast and reliable method of matrix generation. The derivation of equations is presented in the ESI,† and both methods are available through the MQCT suite of codes.[42,43] A new version of our code, MQCT_2023, will be made available to the community soon.[69] In the present version of the MQCT program, all summations in eqn (14) are done numerically. In principle, using angular momentum coupling, summations over projection quantum numbers can be done analytically, resulting in an expression with a 9j symbol.[70] Such a method may offer an additional computational speed up and will be explored in the future.

Calculations of energy dependencies of inelastic cross sections were carried out for a large set of state-to-state transitions in ND_3 + D_2, as presented in the ESI.† It was concluded that the principle of microscopic reversibility is satisfied by MQCT calculations in a broad range of energies, except maybe at the lowest energies, which is not so surprising for an approximate quantum/classical theory. But even in those cases when the deviations from reversibility are observed, they remain manageable (small). We did not find any transition for which the results of MQCT would violate reversibility badly. This concerns transitions of all kinds: when both ND_3 and D_2 molecules are excited or both are quenched, when one is excited while the other is quenched and *vice versa*, when the ND_3 state changes its parity (*i.e.*, a nearly elastic transition between rotationally degenerate states) while D_2 is excited or quenched, and when ND_3 is excited or quenched while D_2 remains in the same state, ground or excited. In all these processes the results of MQCT were found to satisfy the principle of microscopic reversibility.

The analysis of opacity functions (the dependence of inelastic transition probability on the collision impact parameter) showed that state-to-state transition processes actively utilize two complementary pathways: potential-driven transitions described by the state-to-state transition matrix (within the same m-components) and Coriolis-driven transitions (between different m-components) that occur in the body-fixed reference frame that rotates during the process of molecule–molecule collision. Transition probabilities that correspond to two pathways exhibit different behaviors (as a function of collision impact parameter) with Coriolis-driven processes being somewhat weaker and vanishing completely for head on collisions (zero impact parameter).

A very instructive time-dependent insight was obtained by monitoring the evolution of state populations along MQCT trajectories, for several representative initial conditions. In particular, it was shown that when the initial state of D_2 is its ground state $j = 0$, the excitation of ND_3 rotational states proceeds indirectly through the excited $j = 2$ state of D_2. In this two-step process the kinetic energy of molecule–molecule collision is first used to excite D_2 ($j = 2$) and only then is transferred to the excited rotational states of ND_3. This scenario is presented in the TOC image.

The comparison of our MQCT results with the full-quantum results from the literature was presented. It was demonstrated that the values of MQCT cross sections follow all trends seen in the full-quantum calculations and are just slightly smaller, by 8% on average. This very good performance of MQCT is encouraging. It opens new opportunities for the theoretical description of molecule–molecule collisional energy exchange, since MQCT calculations are quite affordable and offer a very useful time-dependent insight.

Conflicts of interest

There are no conflicts to declare.

Acknowledgements

This research was supported by the NSF Chemistry program, grant number CHE-2102465. We used resources of the National Energy Research Scientific Computing Center, which is supported by the Office of Science of the U.S. Department of Energy under Contract No. DE-AC02-5CH11231. Also, we used HPC resources at Marquette funded in part by the National Science foundation award CNS-1828649. Dr Ad Van der Avoird and Dr Gerrit C. Groenenboom are acknowledged for stimulating discussions and their continuous support for this project. C. Joy acknowledges support from Schmitt Fellowship at Marquette. B. Mandal acknowledge the support of Denis J. O'Brien and Eisch Fellowships at Marquette. D. Bostan acknowledge the support of the Eisch Fellowship and Bournique Award at Marquette.

References

1 J. A. Miller, R. Sivaramakrishnan, Y. Tao, C. F. Goldsmith, M. P. Burke, A. W. Jasper, N. Hansen, N. J. Labbe,

P. Glarborg and J. Zádor, Combustion chemistry in the twenty-first century: developing theory-informed chemical kinetics models, *Prog. Energy Combust. Sci.*, 2021, **83**, 100886.
2 J. Cho, Y. Tao, Y. Georgievskii, S. J. Klippenstein, A. W. Jasper and R. Sivaramakrishnan, The role of collisional energy transfer in the thermal and prompt dissociation of 1-methyl allyl, *Proc. Combust. Inst.*, 2022, **78**, 1540–7489.
3 S. J. McGurk, J. B. Halpern, K. G. McKendrick and M. L. Costen, Parity-Dependent Rotational Energy Transfer in $CN(A^2\Pi, \nu = 4, jF_1\varepsilon)$ + N_2, O_2, and CO_2 Collisions, *J. Phys. Chem. A*, 2014, **118**, 2007–2017.
4 J. Cho, A. W. Jasper, Y. Georgievskii, S. J. Klippenstein and R. Sivaramakrishnan, The role of energy transfer and competing bimolecular reactions in characterizing the unimolecular dissociations of allylic radicals, *Combust. Flame*, 2022, **112**, 0010–2180.
5 R. L. Macdonald, E. Torres, T. E. Schwartzentruber and M. Panesi, State-to-state master equation and direct molecular simulation study of energy transfer and dissociation for the N_2–N system, *J. Phys. Chem. A*, 2020, **124**, 6986–7000.
6 S. Sur, S. A. Ndengué, E. Quintas-Sánchez, C. Bop, F. Lique and R. Dawes, Rotationally inelastic scattering of O_3–Ar: state-to-state rates with the multiconfigurational time dependent Hartree method, *Phys. Chem. Chem. Phys.*, 2020, **22**, 1869–1880.
7 J. A. Miller and S. J. Klippenstein, Master equation methods in gas phase chemical kinetics, *J. Phys. Chem. A*, 2006, **110**, 10528–10544.
8 M. L. Dubernet and E. Quintas-Sánchez, First quantum study of the rotational excitation of HCN by *para*-H_2O: convergence of quantum results, influence of the potential energy surface, and approximate rate coefficients of interest for cometary atmospheres, *Mol. Astrophys.*, 2019, **16**, 100046.
9 B. Mandal, A. Semenov and D. Babikov, Adiabatic Trajectory Approximation within the Framework of Mixed Quantum/Classical Theory, *J. Phys. Chem. A*, 2020, **124**, 9877–9888.
10 B. Mandal, C. Joy, A. Semenov and D. Babikov, Mixed Quantum/Classical Theory for Collisional Quenching of PAHs in the Interstellar Media, *ACS Earth Space Chem.*, 2022, **6**, 521–529.
11 M. Besemer, G. Tang, Z. Gao, A. van der Avoird, G. C. Groenenboom, S. Y. T. van de Meerakker and T. Karman, Glory scattering in deeply inelastic molecular collisions, *Nat. Chem.*, 2022, **14**, 664–669.
12 W. Allison and B. Feuerbacher, Rotationally Inelastic Molecule-Surface Scattering, *Phys. Rev. Lett.*, 1980, **45**, 2040.
13 G. D. Billing, Inelastic scattering and chemisorption of CO on a Pt(111) surface, *Chem. Phys.*, 1984, **86**, 349–359.
14 O. Bünermann, A. Kandratsenka and A. M. Wodtke, Inelastic scattering of H atoms from surfaces, *J. Phys. Chem. A*, 2021, **125**, 3059–3076.
15 S. B. M. Bosio and W. L. Hase, Energy transfer in rare gas collisions with self-assembled monolayers, *J. Chem. Phys.*, 1997, **107**, 9677–9686.
16 S. Chhabra, M. Gacesa, M. S. Khalil, A. Al Ghaferi and N. El-Kork, A quantum-mechanical investigation of $O(^3P)$ + CO scattering cross sections at superthermal collision energies, *Mon. Not. R. Astron. Soc.*, 2023, **519**, 1253–1260.
17 R. Padash and S. Ramazani, Collision processes, dynamic and kinetic parameters, and energy exchanges of particles in astrochemistry reaction of NH + H_2 and deuterated analogs on an interpolated potential energy surface, *Mol. Astrophys.*, 2020, **20**, 100085.
18 S. Falcinelli, J. M. Farrar, F. Vecchiocattivi and F. Pirani, Quantum-state controlled reaction channels in chemi-ionization processes: radiative (optical–physical) and exchange (oxidative–chemical) mechanisms, *Acc. Chem. Res.*, 2020, **53**, 2248–2260.
19 M. Kirste, X. Wang, H. C. Schewe, G. Meijer, K. Liu, A. van der Avoird, L. M. C. Janssen, K. B. Gubbels, G. C. Groenenboom and S. Y. T. van de Meerakker, Quantum-state resolved bimolecular collisions of velocity-controlled OH with NO radicals, *Science*, 2012, **338**, 1060–1063.
20 Z. Gao, S. N. Vogels, M. Besemer, T. Karman, G. C. Groenenboom, A. van der Avoird and S. Y. T. van de Meerakker, State-to-state differential cross sections for inelastic collisions of NO radicals with *para*-H_2 and *ortho*-D_2, *J. Phys. Chem. A*, 2017, **121**, 7446–7454.
21 P. Warneck and J. Williams, Gas-Phase Photochemistry, *The Atmospheric Chemist's Companion: Numerical Data for Use in the Atmospheric Sciences*, 2012, 189–225.
22 Y. Lee, M. R. Combi, V. Tenishev, S. W. Bougher and R. J. Lillis, Hot oxygen corona at Mars and the photochemical escape of oxygen: improved description of the thermosphere, ionosphere, and exosphere, *J. Geophys. Res. Planets*, 2015, **120**, 1880–1892.
23 S. Chhabra, A. Kushwaha, R. Kaur and T. J. D. Kumar, Ultracold rotational quenching of NCCN scattering with ^{3}He and ^{4}He, *Chem. Phys. Lett.*, 2020, **738**, 136819.
24 J. Huang, S. Liu, D. H. Zhang and R. V. Krems, Time-dependent wave packet dynamics calculations of cross sections for ultracold scattering of molecules, *Phys. Rev. Lett.*, 2018, **120**, 143401.
25 G. Quéméner, N. Balakrishnan and R. V. Krems, Vibrational energy transfer in ultracold molecule–molecule collisions, *Phys. Rev. A: At., Mol., Opt. Phys.*, 2008, **77**, 30704.
26 S. F. Dos Santos, N. Balakrishnan, R. C. Forrey and P. C. Stancil, Vibration–vibration and vibration–translation energy transfer in H_2–H_2 collisions: a critical test of experiment with full-dimensional quantum dynamics, *J. Chem. Phys.*, 2013, **138**, 104302.
27 N. Bouhafs, C. Rist, F. Daniel, F. Dumouchel, F. Lique, L. Wiesenfeld and A. Faure, Collisional excitation of NH_3 by atomic and molecular hydrogen, *Mon. Not. R. Astron. Soc.*, 2017, **470**, 2204–2211.
28 G. Tang, M. Besemer, J. Onvlee, T. Karman, A. van der Avoird, G. C. Groenenboom and S. Y. T. van de Meerakker, Correlated rotational excitations in NO–CO inelastic collisions, *J. Chem. Phys.*, 2022, **156**, 214304.
29 M. Żółtowski, J. Loreau and F. Lique, Collisional energy transfer in the CO–CO system, *Phys. Chem. Chem. Phys.*, 2022, **24**, 11910–11918.

30 I. V. Tarabukin, L. A. Surin, M. Hermanns, B. Heyne, S. Schlemmer, K. L. K. Lee, M. C. McCarthy and A. van der Avoird, Rotational spectroscopy and bound state calculations of deuterated NH_3–H_2 van der Waals complexes, *J. Mol. Spectrosc.*, 2021, **377**, 111442.
31 Q. Ma, A. der Avoird, J. Loreau, M. H. Alexander, S. Y. T. van de Meerakker and P. J. Dagdigian, Resonances in rotationally inelastic scattering of NH_3 and ND_3 with H_2, *J. Chem. Phys.*, 2015, **143**, 44312.
32 A. Faure, L. Wiesenfeld, M. Wernli and P. Valiron, The role of rotation in the vibrational relaxation of water by hydrogen molecules, *J. Chem. Phys.*, 2005, **123**, 104309.
33 A. Rodríguez-Fernández, L. Bonnet, C. Crespos, P. Larrégaray and R. Díez Muiño, When Classical Trajectories Get to Quantum Accuracy: The Scattering of H_2 on Pd(111), *J. Phys. Chem. Lett.*, 2019, **10**, 7629–7635.
34 L. Guo, W. Wang, Y. Liu, D. Ma, C. Xu and Y. Zhou, Quasiclassical trajectory study of inelastic collision energy transfer between H_2CO and H_2 on a full-dimensional potential energy surface, *Chem. Phys. Lett.*, 2021, **781**, 139014.
35 A. Faure, N. Crimier, C. Ceccarelli, P. Valiron, L. Wiesenfeld and M. L. Dubernet, Quasi-classical rate coefficient calculations for the rotational (de) excitation of H_2O by H_2, *Astron. Astrophys.*, 2007, **472**, 1029–1035.
36 L. A. Surin, I. V. Tarabukin, S. Schlemmer, A. A. Breier, T. F. Giesen, M. C. McCarthy and A. van der Avoird, Rotational spectroscopy of the NH_3–H_2 molecular complex, *Astrophys. J.*, 2017, **838**, 27.
37 M. Ben Khalifa, E. Quintas-Sánchez, R. Dawes, K. Hammami and L. Wiesenfeld, Rotational quenching of an interstellar gas thermometer: $CH_3CN\cdots He$ collisions, *Phys. Chem. Chem. Phys.*, 2020, **22**, 17494–17502.
38 J. Loreau and A. der Avoird, Scattering of NH_3 and ND_3 with rare gas atoms at low collision energy, *J. Chem. Phys.*, 2015, **143**, 184303.
39 K. B. Gubbels, S. Y. T. van de Meerakker, G. C. Groenenboom, G. Meijer and A. van der Avoird, Scattering resonances in slow NH_3–He collisions, *J. Chem. Phys.*, 2012, **136**, 74301.
40 Z. Gao, J. Loreau, A. Van Der Avoird and S. Y. T. Van, De Meerakker, Direct observation of product-pair correlations in rotationally inelastic collisions of ND_3 with D_2, *Phys. Chem. Chem. Phys.*, 2019, **21**, 14033–14041.
41 L. Wiesenfeld, Quenching transitions for the rovibrational transitions of water: *ortho*-H_2O in collision with *ortho*-and *para*-H_2, *J. Chem. Phys.*, 2022, **157**, 174304.
42 B. Mandal, C. Joy, D. Bostan, A. Eng and D. Babikov, Adiabatic Trajectory Approximation: A New General Method in the Toolbox of Mixed Quantum/Classical Theory for Collisional Energy Transfer, *J. Phys. Chem. Lett.*, 2023, **14**, 817–824.
43 A. Semenov, B. Mandal and D. Babikov, MQCT: user-ready program for calculations of inelastic scattering of two molecules, *Comput. Phys. Commun.*, 2020, **252**, 107155.
44 W. H. Miller, W. L. Hase and C. L. Darling, A simple model for correcting the zero point energy problem in classical trajectory simulations of polyatomic molecules, *J. Chem. Phys.*, 1989, **91**, 2863–2868.
45 G. Czakó, A. L. Kaledin and J. M. Bowman, A practical method to avoid zero-point leak in molecular dynamics calculations: application to the water dimer, *J. Chem. Phys.*, 2010, **132**, 164103.
46 J. M. Bowman, B. Gazdy and Q. Sun, A method to constrain vibrational energy in quasiclassical trajectory calculations, *J. Chem. Phys.*, 1989, **91**, 2859–2862.
47 F. Brieuc, Y. Bronstein, H. Dammak, P. Depondt, F. Finocchi and M. Hayoun, Zero-Point Energy Leakage in Quantum Thermal Bath Molecular Dynamics Simulations, *J. Chem. Theory Comput.*, 2016, **12**, 5688–5697.
48 G. D. Billing, The semiclassical treatment of molecular roto/vibrational energy transfer, *Comput. Phys. Rep.*, 1984, **1**, 239–296.
49 G. D. Billing, *The quantum classical theory*, Oxford University Press, New York, 2003.
50 A. Semenov and D. Babikov, Inelastic Scattering of Identical Molecules within Framework of the Mixed Quantum/Classical Theory: Application to Rotational Excitations in H_2 + H_2, *J. Phys. Chem. A*, 2016, **120**, 3861–3866.
51 A. Semenov and D. Babikov, Mixed Quantum/Classical Theory for Molecule–Molecule Inelastic Scattering: Derivations of Equations and Application to N_2 + H_2 System, *J. Phys. Chem. A*, 2015, **119**, 12329–12338.
52 A. Semenov and D. Babikov, Mixed quantum/classical calculations of total and differential elastic and rotationally inelastic scattering cross sections for light and heavy reduced masses in a broad range of collision energies, *J. Chem. Phys.*, 2014, **140**, 44306.
53 A. Semenov, M. Ivanov and D. Babikov, Ro-vibrational quenching of CO (v = 1) by He impact in a broad range of temperatures: a benchmark study using mixed quantum/classical inelastic scattering theory, *J. Chem. Phys.*, 2013, **139**, 74306.
54 A. Semenov, M. L. Dubernet and D. Babikov, Mixed quantum/classical theory for inelastic scattering of asymmetric-top-rotor + atom in the body-fixed reference frame and application to the H_2O + He system, *J. Chem. Phys.*, 2014, **141**, 114304.
55 A. Semenov and D. Babikov, Mixed Quantum/Classical Approach for Description of Molecular Collisions in Astrophysical Environments, *J. Phys. Chem. Lett.*, 2015, **6**, 1854–1858.
56 A. Semenov and D. Babikov, MQCT. I. Inelastic Scattering of Two Asymmetric-Top Rotors with Application to H_2O + H_2O, *J. Phys. Chem. A*, 2017, **121**, 4855–4867.
57 C. Boursier, B. Mandal, D. Babikov and M. L. Dubernet, New H_2O–H_2O collisional rate coefficients for cometary applications, *Mon. Not. R. Astron. Soc.*, 2020, **498**, 5489–5497.
58 A. T. J. B. Eppink and D. H. Parker, Velocity map imaging of ions and electrons using electrostatic lenses: application in photoelectron and photofragment ion imaging of molecular oxygen, *Rev. Sci. Instrum.*, 1997, **68**, 3477–3484.
59 M. A. Morrison and G. A. Parker, A Guide to Rotations in Quantum Mechanics, *Aust. J. Phys.*, 1987, **40**, 465–497.
60 D. A. Varshalovich, A. N. Moskalev and V. K. Khersonskii, *Quantum Theory of Angular Momentum*, World scientific, 1988.
61 R. N. Zare and W. G. Harter, Angular Momentum: Understanding Spatial Aspects in Chemistry and Physics, *Phys. Today*, 1989, **42**, 68.

62 D. M. Brink, G. R. Satchler and M. Danos, Angular Momentum, *Phys. Today*, 1963, **16**, 80.
63 A. R. Edmonds and H. Mendlowitz, Angular Momentum in Quantum Mechanics, *Phys. Today*, 1958, **11**, 34.
64 S. Green, Energy transfer in NH_3–He collisions, *J. Chem. Phys.*, 1980, **73**, 2740–2750.
65 G. C. Groenenboom, Angular momentum theory, *Quantum theoretical chemistry (NWI-MOL112)*, Radboud University, Nijmegen, the Netherlands, 2023, pp. 38–49.
66 P. S. Z. Żuchowski and J. M. Hutson, Low-energy collisions of NH_3 and ND_3 with ultracold Rb atoms, *Phys. Rev. A: At., Mol., Opt. Phys.*, 2009, **79**, 62708.
67 J. Schleipen and J. J. ter Meulen, State-to-state cross sections for rotational excitation of *ortho*- and *para*-NH_3 by He and H_2, *Chem. Phys.*, 1991, **156**, 479–496.
68 A. Semenov and D. Babikov, Mixed quantum/classical theory of rotationally and vibrationally inelastic scattering in space-fixed and body-fixed reference frames, *J. Chem. Phys.*, 2013, **139**, 174108.
69 MarquetteQuantum, **https://github.com/MarquetteQuantum** (accessed May 2023).
70 A. van der Avoird, P. E. S. Wormer and R. Moszynski, From intermolecular potentials to the spectra of van der Waals molecules, and *vice versa*, *Chem. Rev.*, 1994, **94**, 1931–1974.